

# Source quantification by mobile gamma-ray spectrometry systems: A Bayesian approach

David Breitenmoser<sup>1,2\*</sup>, Alberto Stabilini<sup>1</sup>, Małgorzata Magdalena Kasprzak<sup>1</sup>,  
Sabine Mayer<sup>1</sup>

<sup>1</sup>Department of Radiation Safety and Security, Paul Scherrer Institute (PSI),  
Forschungsstrasse 111, Villigen PSI, AG 5232, Switzerland.

<sup>2</sup>Department of Nuclear Engineering & Radiological Sciences, University of Michigan, 2355  
Bonisteel Blvd., Ann Arbor, MI 48109-2104, United States of America.

\*Corresponding author(s). E-mail(s): [david.breitenmoser@psi.ch](mailto:david.breitenmoser@psi.ch);  
Contributing authors: [alberto.stabilini@psi.ch](mailto:alberto.stabilini@psi.ch); [malgorzata.kasprzak@psi.ch](mailto:malgorzata.kasprzak@psi.ch);  
[sabine.mayer@psi.ch](mailto:sabine.mayer@psi.ch);

## Abstract

Accurately quantifying gamma-ray sources from mobile gamma-ray spectrometry surveys has remained a fundamentally elusive, long-standing inverse problem at the interface of nuclear and computational physics. Here, we present a full-spectrum Bayesian inference framework that resolves this inverse problem by combining high-fidelity, platform-dynamic Monte Carlo template generation with Bayesian inversion. Applying this methodology to airborne measurements benchmarked against laboratory and *in-situ* ground truths, we demonstrate accurate and robust quantification of both natural and anthropogenic radionuclides under field conditions. By improving activity estimates by an order of magnitude, providing principled uncertainty quantification, and rigorously accounting for overdispersion, this framework opens the way to a more statistically rigorous and physics-informed era of mobile gamma-ray spectrometry, unlocking enhanced inference capabilities in emergency response, environmental monitoring, nuclear security, and planetary exploration.

**Keywords:** Bayesian inference, Monte Carlo simulation, gamma-ray spectroscopy, radiological emergency response, Markov Chain Monte Carlo

## 1 Introduction

Mobile gamma-ray spectrometry (MGRS) has emerged as a powerful technique for detecting and characterizing gamma-ray sources in diverse environments. By deploying spectrometers on ground-based, airborne, marine, and spaceborne platforms, MGRS enables rapid source localization, identification, and quantification in a wide range of fields, including environmental monitoring of marine ecosystems [1, 2], mapping radioactive contamination

after nuclear accidents [3–7], nuclear security and nonproliferation [8–13], geophysics [14–22], and planetary science [23–30]. More recently, the advent of unmanned mobile platforms has opened new opportunities to deploy MGRS systems in previously inaccessible or hazardous environments, further broadening its scope of application [31–35].

While MGRS has shown promising source localization and identification capabilities, quantifying gamma-ray sources has proven a much more challenging task. In contrast to *in-situ* or laboratory settings, MGRS systems operate in a near real-time data acquisition mode with typical sampling frequencies on the order of  $\mathcal{O}(1)$  Hz and source–detector distances ranging from  $\mathcal{O}(10^2)$  m in terrestrial surveys to at least  $\mathcal{O}(10^5)$  m for spaceborne platforms. Consequently, inferring source strengths from MGRS data constitutes a severely ill-posed inverse problem. The combination of low-count statistics, dynamically varying source–detector geometries, and strong spectral correlations between different radionuclides leads to non-uniqueness and instability in the solution space. To address this ill-posed inverse problem, the sparse and low-count spectra characteristic of most MGRS systems preclude the use of conventional peak-fitting methods, which are effective only in stationary or otherwise well-controlled source–detector settings, such as prolonged planetary surveys [24, 25, 29, 30]. Instead, template-matching approaches, commonly referred to as full-spectrum analysis (FSA), have emerged as the most viable alternative, and have demonstrated promising results in both terrestrial [36–40] and spaceborne applications [23, 26, 28]. However, current FSA implementations remain limited by systematic biases in the inferred source strengths and reduced sensitivity under the low-count conditions characteristic for single-pass MGRS surveys [28, 41–43].

We attribute these limitations of current FSA implementations to two primary factors: inaccuracies in spectral-template generation and limitations of the statistical models employed in the inversion. On the template side, empirical calibration libraries are necessarily sparse, restricted to a limited range of radionuclide sources and source–detector configurations, and their extension to broader survey conditions is prohibitively costly and time-consuming, often requiring days of dedicated measurements and expensive source handling [44–46]. Moreover, empirical templates are unavoidably affected by variable background contributions, introducing additional systematic uncertainties. Numerically generated templates, by contrast, offer much broader flexibility but historically have relied on oversimplified Monte Carlo models in which the mobile platforms were either neglected entirely or represented by primitive geometries to reduce the model complexity and computational costs [6, 12, 13, 21, 42, 47–50]. These approximations fail to reproduce key platform-dependent effects such as scattering and attenuation within the platform structure, resulting in persistent, energy-dependent template biases that can exceed 200% at photon energies below  $\sim 100$  keV [12, 47, 50]. Recent advances in high-fidelity Monte Carlo modeling have demonstrated that incorporating detailed dynamic mass models into the simulations can substantially reduce template-related discrepancies [51, 52].

The second source of systematic error arises from the inversion framework itself. Most existing FSA pipelines adopt frequentist formulations based on maximum likelihood estimation (MLE) algorithms combined with Gaussian likelihoods [21, 23, 36–38, 53–55]. While computationally efficient, these approaches are formally inconsistent with the sparse statistics of MGRS data and tend to produce biased estimates and unreliable uncertainty quantification under low-count conditions [56–58]. To address this mismatch, Poisson-based MLE formulations have been proposed [10, 11, 13]. These models better reflect the discrete nature of count data, yet they remain limited in several respects: they generally do not account for overdispersion effects that arise from fluctuating experimental conditions inherent in MGRS surveys, they provide no rigorous framework for uncertainty quantification, and they are typically restricted to inferring only a small number of sources, often requiring ad hoc regularization to stabilize solutions. These limitations motivate the development of alternative inference strategies that rigorously capture the underlying count statistics, support robust inversion for an arbitrary number of sources, and provide a principled and transparent framework for uncertainty quantification.

In this work, we introduce an alternative methodology for MGRS source quantification that addresses the limitations of current FSA implementations by combining high-fidelity numerical template generation with a

Bayesian inversion framework. The numerical templates leverage detailed, dynamically updated Monte Carlo models of the measurement platform to accurately predict spectral responses across a wide range of source-detector configurations. Simultaneously, the Bayesian inversion rigorously accounts for the underlying statistics of sparse MGRS data, enabling estimation of source strengths for an arbitrary number of radionuclides while providing a robust framework for uncertainty quantification. We evaluate the proposed methodology on a series of dedicated MGRS measurements benchmarked against laboratory and *in-situ* reference data, achieving accurate and reliable quantification of both natural and anthropogenic radionuclides for short, sparse acquisitions  $\mathcal{O}(1)$  s as well as for prolonged measurements  $\mathcal{O}(10^2)$  s affected by significant overdispersion due to environmental and platform variability. By resolving systematic template biases, properly accounting for sparse and overdispersed count statistics, and supporting robust inversion for multiple sources, this framework overcomes key limitations of current FSA implementations and establishes a generalizable approach for next-generation MGRS applications in radiological emergency response, planetary exploration, nuclear security, and geophysics.

## 2 Results

### 2.1 Full-spectrum Bayesian inference framework

As illustrated in [Fig. 1](#), our proposed FSA methodology combines MGRS pulse-height spectral data with high-performance computing (HPC) based template generation in a unified Bayesian framework. Bayesian inference offers a natural, consistent, and transparent way of combining existing information with empirical data to solve complex inverse problems using a solid probabilistic decision theory framework [68–72]. It has been successfully applied in a wide variety of fields, including physics [69, 71, 73], engineering [74, 75], earth sciences [76, 77], biology and medicine [78, 79], machine learning [80–82], and social sciences [83, 84].

In contrast to traditional frequentist MLE approaches, Bayesian inversion does not infer a single point solution, but rather a probability density function  $\pi(\boldsymbol{\theta} | \mathcal{Y}, \mathcal{D}, \mathcal{F})$  over the  $M$ -dimensional parameter space  $\mathcal{D}_{\boldsymbol{\theta}} = \mathbb{R}^M$ . This posterior distribution is conditional on three components: the set of observed pulse-height spectra  $\mathcal{Y} = \{\mathbf{y}_i \in \mathbb{N}^{N_y} \mid i \in \mathbb{N}_+, i \leq N_y\}$  with  $N \in \mathbb{N}$  channels and  $N_y \in \mathbb{N}$  realizations, the known experimental conditions  $\mathcal{D} = \{\mathbf{d}_k \in \mathbb{R}^{N_{\mathbf{d}}} \mid k \in \mathbb{N}_+, k \leq N_{\mathbf{d}}\}$  under which the spectra were recorded, and the probabilistic forward model  $\mathcal{F}$ . The forward model  $\mathcal{F}$  defines the pulse-height spectra  $\mathbf{y}$  as realizations of a random vector  $\mathbf{Y}$  following a conditional probability density  $\mathcal{F}: \mathbf{Y} \mid \boldsymbol{\theta}, \mathbf{d} \sim \pi(\mathbf{y} \mid \boldsymbol{\theta}, \mathbf{d})$ . Its expectation  $\langle \mathbf{Y} \rangle = \mathcal{M}(\boldsymbol{\theta}, \mathbf{d})$  corresponds to the deterministic forward mapping from any admissible parameter vector  $\boldsymbol{\theta}$  to the expected spectral response under the specified experimental conditions  $\mathbf{d}$ .

Following the FSA approach [85, 86], we define  $\mathcal{M}$  as the linear superposition of spectral templates  $\boldsymbol{\psi} \in \mathbb{R}_+^{N_y}$ , each representing the characteristic full-spectrum response of the MGRS system to a specific gamma-ray source—normalized by the source strength  $\xi \in \mathbb{R}_+$ —under given (time-dependent) experimental conditions  $\mathbf{d}$  during the survey with measurement live time  $\Delta t_{\text{live}}$ :

$$\mathcal{M}(\boldsymbol{\xi}, \mathbf{d}) = \int_0^{\Delta t_{\text{live}}} \mathbf{M}(\mathbf{d}) \boldsymbol{\xi} + \mathbf{c}_b(\mathbf{d}) dt \quad (1)$$

where  $\mathbf{M} \in \mathbb{R}_+^{N_y \times N_{\xi}}$  denotes the spectral template matrix  $\mathbf{M}(\mathbf{d}) := [\boldsymbol{\psi}^{(1)}(\mathbf{d}), \boldsymbol{\psi}^{(2)}(\mathbf{d}), \dots, \boldsymbol{\psi}^{(N_{\xi})}(\mathbf{d})]$ , together with  $\boldsymbol{\xi} \in \mathbb{R}_+^{N_{\xi}}$  specifying the source strength of the  $N_{\xi} \in \mathbb{N}$  gamma-ray sources, and  $\mathbf{c}_b \in \mathbb{R}_+^{N_y}$  encoding the spectral response to nuisance gamma-ray backgrounds.

Using this Bayesian FSA formalism, we compute the posterior distribution by applying Bayes' theorem, which combines the likelihood function  $\mathcal{L}(\boldsymbol{\theta}; \mathcal{Y}, \mathcal{D}) := \prod_{i=1}^{N_y} \pi(\mathbf{y}_i \mid \boldsymbol{\theta}, \mathbf{d}_i)$ , with the prior distribution  $\pi(\boldsymbol{\theta})$  encoding all prior knowledge and physical constraints about the solution space:

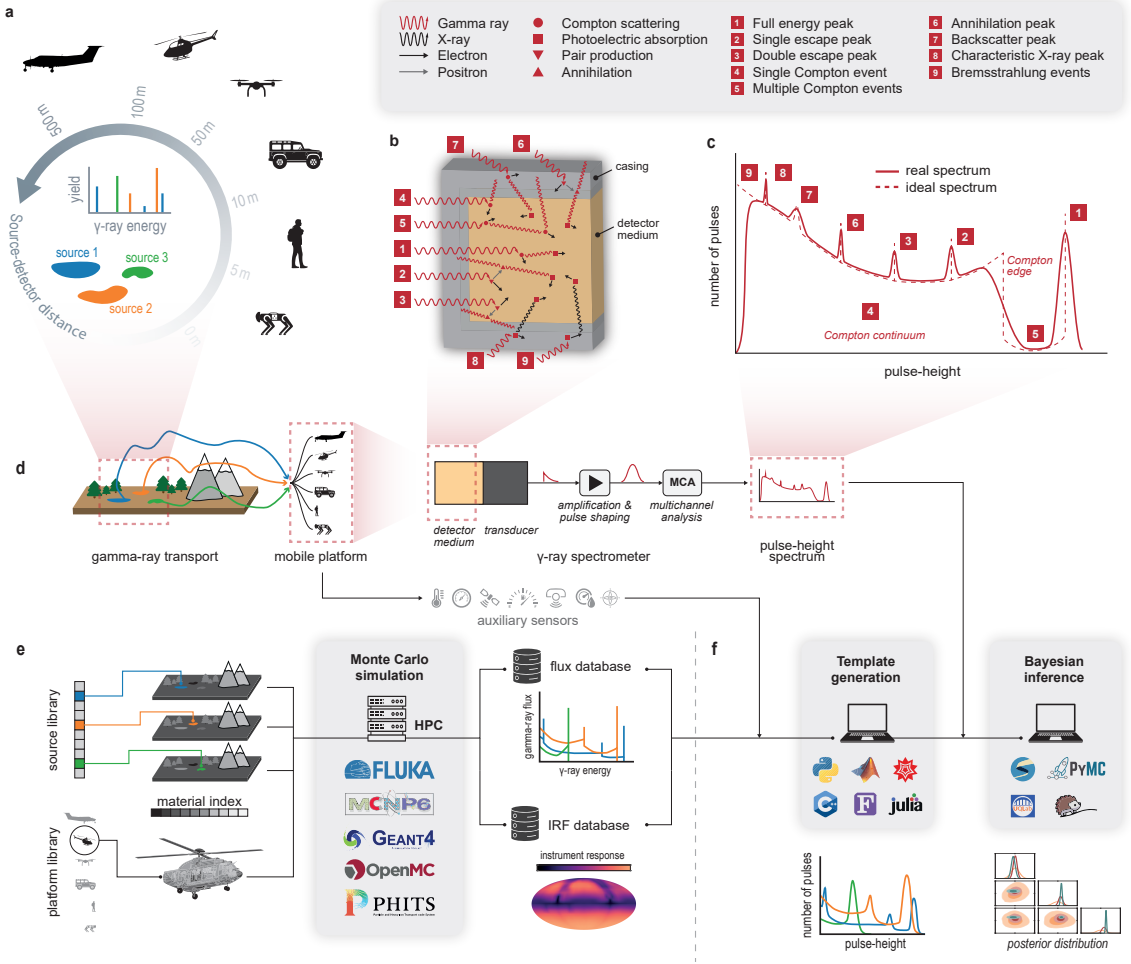


**Fig. 1** Overview of the full-spectrum Bayesian inference framework. **a**, Characteristic source-detector distances for various mobile platforms utilized in MGRS. **b**, Gamma-ray-matter interaction mechanisms and associated secondary processes. **c**, Characteristic spectral features in the full-spectrum pulse-height response to monoenergetic gamma-ray events. **d**, Hierarchical sequence of physical processes involved in MGRS. **e**, Instrument response function (IRF) and double differential gamma-ray flux database generation utilizing high-fidelity radiation transport codes [59–63] run on high-performance computing (HPC) infrastructure. **f**, High-fidelity spectral template generation and Bayesian inference on a local workstation utilizing general-purpose programming languages and dedicated Bayesian numerical codes [64–67].

$$\pi(\boldsymbol{\theta} | \mathcal{Y}, \mathcal{D}, \mathcal{F}) = \frac{\mathcal{L}(\boldsymbol{\theta}; \mathcal{Y}, \mathcal{D}) \pi(\boldsymbol{\theta})}{\int_{\mathcal{D}_{\boldsymbol{\theta}}} \mathcal{L}(\boldsymbol{\theta}; \mathcal{Y}, \mathcal{D}) \pi(\boldsymbol{\theta}) d\boldsymbol{\theta}} \quad (2)$$

with the resulting posterior distribution  $\pi(\boldsymbol{\theta} | \mathcal{Y}, \mathcal{D}, \mathcal{F})$  providing a complete probabilistic description of the solution space  $\mathcal{D}_{\boldsymbol{\theta}}$ .

While Eq. (2) is analytically intractable for general likelihood and prior distributions [70], advances in Bayesian computation over the past decades have made accurate numerical approximations feasible. State-of-the-art algorithms such as Markov chain Monte Carlo (MCMC) [87–91] and nested sampling (NS) [66, 92–96] can

now be readily employed to explore the posterior distribution even in highly complex inverse problems. However, these methods remain computationally demanding, often requiring  $\geq \mathcal{O}(10^4)$  forward model evaluations for a single inference task. Consequently, the development of forward models that can be evaluated rapidly is a key prerequisite for the practical implementation of the proposed Bayesian FSA methodology.

Constructing a forward model  $\mathcal{F}$  that can be evaluated rapidly while retaining predictive accuracy for the full-spectrum MGRS response under varying experimental conditions is a computationally challenging task. As illustrated in [Fig. 1](#), the spectral response of an MGRS system arises from a hierarchical sequence of physical processes: the emission characteristics of multiple gamma-ray sources within the field of view, spanning distances from  $\mathcal{O}(10^1)$  m to  $\mathcal{O}(10^5)$  m; the interactions and propagation of the emitted gamma rays through the environment and the mobile platform, including the generation of secondary X-rays and annihilation photons; and the multiscale energy conversion chain in the detector medium, transducers, and subsequent signal wave processing. As discussed in [Section 1](#), Monte Carlo simulations [\[6, 12, 13, 21, 42, 47–50\]](#) utilizing high-fidelity radiation transport codes [\[59–63\]](#) represent the most established and reliable method for numerically approximating the spectral template matrices in [Eq. \(1\)](#) as a function of the experimental conditions  $\mathfrak{d}$ . Their main drawback, however, is computational cost: high-fidelity simulations typically require  $\Delta t_{MC} = \mathcal{O}(10^4)$  core-hours per spectral template [\[51\]](#). Since template generation scales with both the number of sources  $N_\xi$  and the number of unique experimental states  $N_\gamma$ , brute-force Monte Carlo approaches are prohibitive even for moderate survey sizes ( $N_\xi = \mathcal{O}(10^5)$ ,  $N_\gamma = \mathcal{O}(10^4)$ ), despite access to current HPC infrastructure. To overcome this limitation, we propose a two-stage template generation strategy: (i) precomputing instrument response functions (IRFs) and double-differential gamma-ray flux banks for a set of a priori defined experimental conditions utilizing HPC infrastructure, and (ii) assembling spectral templates from these precomputed components on a local workstation (see [Section 4.1](#)). As demonstrated in our previous work [\[52\]](#), this approach reduces the evaluation cost to  $\mathcal{O}(1)$  s per template, enabling the generation of high-fidelity spectral template matrices  $\mathbf{M}$  at practical computational expense and, in turn, providing a viable pathway to perform full-spectrum Bayesian inference in MGRS.

## 2.2 Data selection

We evaluated the proposed Bayesian methodology on the Swiss Airborne Gamma-Ray Spectrometry (SAGRS) system, a state-of-the-art airborne MGRS platform equipped with a  $\sim 1.7 \times 10^4$  cm<sup>3</sup> NaI(Tl) spectrometer mounted in an Aérospatiale AS332M1 Super Puma helicopter (see [Section 4.4](#)). The system offers both a validated high-fidelity Monte Carlo mass model and a curated archive of systematically collected datasets spanning more than five years in Switzerland and abroad [\[51, 97\]](#), providing a robust basis for benchmarking and validation.

Here, we focus on two specific benchmark measurements that were performed during the **ARM22** exercise at the Thun military training ground (46.753°N, 7.596°E) in Switzerland on June 16, 2022 [\[98\]](#). In these experiments, the SAGRS system was operated in a hover flight mode for  $\sim 5$  min with the helicopter positioned at a ground clearance of  $\sim 90$  m above two separately deployed sealed radionuclide point sources ( $^{137}_{55}\text{Cs}$  and  $^{133}_{56}\text{Ba}$ ), which were positioned on the ground and aligned with the aircraft yaw axis. The campaign was specifically designed for reproducibility and validation. Reference activities for the two anthropogenic sources were provided by laboratory gamma-ray assays performed by the source manufacturer. Natural background activity concentrations of terrestrial  $\text{K}_{\text{nat}}$ ,  $\text{U}_{\text{nat}}$ , and  $\text{Th}_{\text{nat}}$  were constrained by *in-situ* gamma-ray spectroscopy at 23 reference positions across the training ground [\[99\]](#).

Data reduction was performed independently for each acquisition using the post-processing pipeline **RLLSpec** [\[51\]](#). To investigate the effect of data sparsity on the Bayesian inversion results, we aggregated pulse-height spectra for three live times: 1 s, 5 s, and the full acquisition ( $\sim 5$  min). The data reduction was carried out separately for the  $^{133}_{56}\text{Ba}$  and  $^{137}_{55}\text{Cs}$  measurements, yielding six independent datasets: **Ba\_1s**, **Ba\_5s**, **Ba\_5m** and

`Cs_1s`, `Cs_5s`, `Cs_5m`, corresponding to the three live times, respectively. Each dataset comprises the gross-count spectrum  $\mathbf{y} \in \mathbb{N}^{N_y}$ , the measurement live time  $\Delta t_{\text{gr}}$ , and the experimental condition vector  $\mathbf{d} \in \mathbb{R}^{N_d}$  that encodes platform and environmental states relevant to forward modeling: helicopter position and orientation (pose), fuel level, and ambient conditions (air temperature, pressure, humidity). Given the steady-state source-detector configuration, we assume constant mean experimental conditions within each acquisition, while intrinsic variability in these conditions is captured through the overdispersion parameterization described in the following section. Helicopter states were retrieved from onboard auxiliary sensors. Meteorological parameters were taken from the MeteoSwiss automatic weather station on the Thun training ground (WIGOS-ID: 0-20000-0-06731). A complete listing of live times and retrieved experimental-condition values is provided in Supplementary Table S1. Further details on the measurement setup, acquisition, and data processing are available in Ref. [51].

### 2.3 Forward modeling

Following the outlined Bayesian inference framework in Section 2.1, we model the expected events in the pulse-height response  $\langle \mathbf{Y} \rangle = \mathcal{M}(\boldsymbol{\xi}, \mathbf{d})$  of the SAGRS spectrometer as the linear superposition of spectral templates  $\boldsymbol{\psi}$  corresponding to the gamma-ray emitters present: the anthropogenic  $^{137}_{55}\text{Cs}$  and  $^{133}_{56}\text{Ba}$  sources, and the naturally occurring terrestrial radionuclides  $\text{K}_{\text{nat}}$ ,  $\text{Th}_{\text{nat}}$ , and  $\text{U}_{\text{nat}}$  with their progeny.

To reduce template bias in our inference, we generated the spectral templates from high-fidelity IRFs and double-differential flux banks, conditioned on the full experimental context, i.e., platform pose, environmental parameters, etc. (see Section 4.1). We generated the IRFs and flux banks through large-scale coupled photon-electron-positron Monte Carlo simulations using the validated SAGRS mass model [51] and the FLUKA code (v4.2.2) [62, 100, 101] combined with the FLAIR graphical interface [102] on HPC infrastructure (see Sections 4.2 and 4.3). A complete listing of all considered experimental-condition values in these simulations are provided in Supplementary Table S1.

Residual intrinsic, cosmic-ray, and atmospheric radon progeny backgrounds were treated as nuisance sources. We estimated their combined spectral contribution  $\mathbf{c}_b$  in Eq. (1) empirically from independent background flights over Lake Thun at orthometric heights matched to the hover measurements (see Supplementary Fig. S1). Because these flights were conducted within 10 km and less than 1 h of the experiments, we considered them representative of the intrinsic and cosmic background at the training site. To account for spatiotemporal variability in radon progeny concentrations, we included an additional variable radon source term  $\Delta\xi_{\text{Rn-nat}} \in \mathbb{R}$  and inferred it jointly with the other source strengths in the Bayesian analysis (see Section 4.3).

We embed our deterministic forward model  $\mathcal{M}$  into a probabilistic negative binomial model  $\mathcal{F} : \mathbf{Y} \mid \boldsymbol{\theta}, \mathbf{d} \sim \mathcal{NB}(\mathbf{y} \mid \boldsymbol{\theta}, \mathbf{d})$ , which generalizes Poisson statistics by relaxing the variance constraint to  $\text{Var}(\mathbf{Y}) = \langle \mathbf{Y} \rangle + \alpha_{\text{NB}} \langle \mathbf{Y} \rangle^2$  with  $\alpha_{\text{NB}} \in \mathbb{R}_+$  being the dispersion parameter associated with the probabilistic model (see Section 4.5). Overdispersion arises because experimental conditions typically fluctuate during the measurement, introducing additional variability in the data and resulting in significant biases if unaccounted for [103–105]. Similar to the radon source term, we infer the dispersion parameter  $\alpha_{\text{NB}}$  jointly with the other source strengths to avoid biased estimates. The resulting inverse problems are six-dimensional, with parameter vectors  $\boldsymbol{\theta} := [\xi_{\text{Ba-133}}, \xi_{\text{K-nat}}, \xi_{\text{Th-nat}}, \xi_{\text{U-nat}}, \Delta\xi_{\text{Rn-nat}}, \alpha_{\text{NB}}]$  for the  $^{133}_{56}\text{Ba}$  related datasets and  $\boldsymbol{\theta} := [\xi_{\text{Cs-137}}, \xi_{\text{K-nat}}, \xi_{\text{Th-nat}}, \xi_{\text{U-nat}}, \Delta\xi_{\text{Rn-nat}}, \alpha_{\text{NB}}]$  for the  $^{137}_{55}\text{Cs}$  related datasets.

### 2.4 Bayesian inversion

We solve the inverse problems for each of the six datasets retrieved in Section 2.2 independently, using the Bayesian inversion framework outlined in Section 2.1. Specifically, we sample the posterior distribution via Bayes' theorem in Eq. (2) using an affine-invariant ensemble MCMC algorithm [91] (see Section 4.5). We present the results from these Bayesian computations as posterior predictive distributions in Fig. 2 alongside univariate and bivariate marginal posterior distributions shown in Fig. 3. In addition, a comprehensive summary

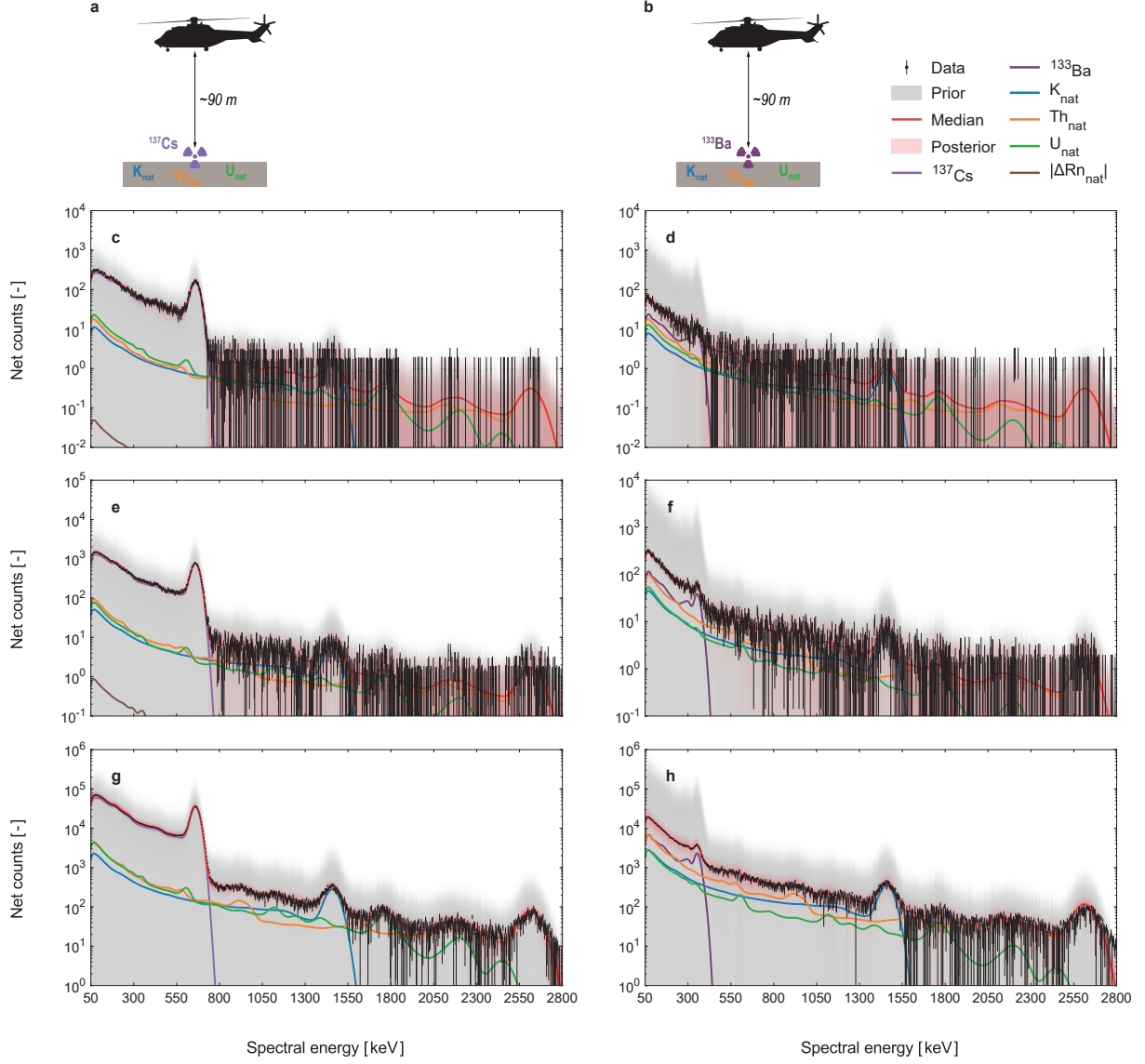


**Fig. 2 Posterior predictive distribution results.** Prior and posterior predictive distributions are shown alongside the measured pulse-height spectra for two measurement configurations: **a**, Hover flight above an anthropogenic  $^{137}_{55}\text{Cs}$  source. **b**, Hover flight above an anthropogenic  $^{133}_{56}\text{Ba}$  source. Results are displayed for all six datasets acquired from these measurements with variable live times of 1 s (**c**, **Cs\_1s**, **d**, **Ba\_1s**), 5 s (**e**, **Cs\_5s**, **f**, **Ba\_5s**), and the full acquisition  $\sim 5$  min (**g**, **Cs\_5m**, **h**, **Ba\_5m**). Uncertainties in the measured pulse-height spectra are shown as 1 standard error (SE) error bars. Posterior predictive distributions are accompanied by point predictions based on the posterior median estimates. Spectral signatures scaled by the posterior median source strengths and measurement live time are also indicated for all sources included in the forward model, namely the anthropogenic  $^{137}_{55}\text{Cs}$  and  $^{133}_{56}\text{Ba}$  sources; the three natural terrestrial radionuclides  $\text{K}_{\text{nat}}$ ,  $\text{Th}_{\text{nat}}$ , and  $\text{U}_{\text{nat}}$ ; and the absolute radon source term  $|\Delta\text{Rn}_{\text{nat}}|$  (partially visible in **c** and **e**). For better interpretability, all spectral quantities were corrected for nuisance backgrounds described in Section 2.3.

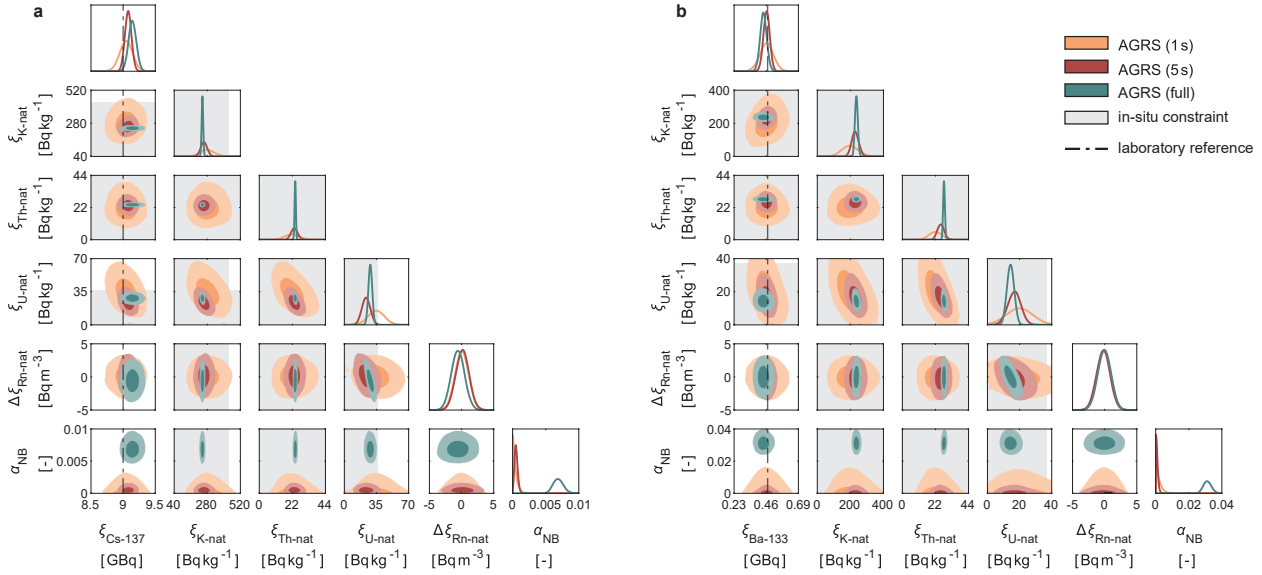


**Fig. 3 Posterior distribution results.** Posterior distributions are shown for two measurement configurations: **a**, Hover flight above an anthropogenic  $^{137}\text{Cs}$  source. **b**, Hover flight above an anthropogenic  $^{133}\text{Ba}$  source. Results are displayed for all six datasets acquired from these measurements with live times of 1 s ( $\text{Cs\_1s}$ ,  $\text{Ba\_1s}$ ), 5 s ( $\text{Cs\_5s}$ ,  $\text{Ba\_5s}$ ), and  $\sim 5$  min ( $\text{Cs\_5m}$ ,  $\text{Ba\_5m}$ ). Each subfigure shows posterior distributions for the related model parameters: source activities of the anthropogenic  $^{137}\text{Cs}$  and  $^{133}\text{Ba}$  point sources ( $\xi_{\text{Cs-137}}$ ,  $\xi_{\text{Ba-133}}$ ); activity mass concentrations of the three natural terrestrial radionuclides  $\text{K}_{\text{nat}}$ ,  $\text{Th}_{\text{nat}}$ , and  $\text{U}_{\text{nat}}$  ( $\xi_{\text{K-nat}}$ ,  $\xi_{\text{Th-nat}}$ ,  $\xi_{\text{U-nat}}$ ); activity volume concentration of the radon source term  $\Delta R_{\text{n-nat}}$  ( $\Delta\xi_{\text{Rn-nat}}$ ), as well as the dispersion parameter of the negative binomial distribution ( $\alpha_{\text{NB}}$ ). Off-diagonal panels depict bivariate posterior marginals with 68% and 99% probability contours, while diagonal panels show the corresponding univariate marginals. Gray-shaded regions indicate *in-situ* gamma-ray spectroscopy constraints on terrestrial radionuclide activity concentrations, and black dashed lines mark best-estimate laboratory gamma-ray assay activities for the two anthropogenic sources.

of posterior point and dispersion estimates for all six datasets is provided in Supplementary Tables S3 and S4 in the Supplementary Information File for this study.

In Fig. 2, we find that the posterior predictive distributions align closely with the measured pulse-height spectra across all datasets. As expected for an identifiable probabilistic model, the dispersion of the posterior predictive distributions decreases substantially relative to the prior predictive ones, reflecting the information gained from the acquired data. This effect is most pronounced for the high-count datasets  $\text{Cs\_5m}$  and  $\text{Ba\_5m}$ . For the shorter acquisitions ( $\text{Cs\_1s}$ ,  $\text{Cs\_5s}$ ,  $\text{Ba\_1s}$ ,  $\text{Ba\_5s}$ ), increased data sparsity results in a weaker reduction in dispersion, particularly at higher spectral energies. These trends are corroborated by the posterior distributions in Fig. 3, which show a corresponding narrowing of credible regions with increasing measurement live time.

While the absolute dispersion in the measured pulse-height spectra shown in Fig. 2 decreases with increasing measurement time, the event-by-event statistical variance relative to the mean in the posterior predictive distributions exhibits an opposite trend. Quantitatively, we observe statistically significant elevations in the dispersion parameter in Fig. 3 for the 5 min datasets compared to the shorter 1 s and 5 s datasets. Specifically, we retrieve posterior median dispersion parameters  $\alpha_{\text{NB}} = 6.87^{+1.58}_{-1.31} \times 10^{-3}$  for  $\text{Cs\_5m}$  and  $\alpha_{\text{NB}} = 3.12^{+0.49}_{-0.43} \times 10^{-2}$  for  $\text{Ba\_5m}$  (95% central credible interval bounds). By contrast, the shorter-duration datasets show substantially lower overdispersion,  $\alpha_{\text{NB}} = [2.78^{+10.62}_{-2.68} \times 10^{-4}, 5.10^{+5.50}_{-3.66} \times 10^{-4}]$  for [ $\text{Cs\_1s}, \text{Cs\_5s}$ ]

and  $\alpha_{\text{NB}} = [1.38^{+5.43}_{-1.33} \times 10^{-3}, 6.57^{+17.73}_{-6.22} \times 10^{-4}]$  for **[Ba\_1s, Ba\_5s]**, consistent with near-Poisson statistics. These results highlight a clear temporal dependence of overdispersion in our measurements. We interpret the elevated overdispersion at longer sampling times as a manifestation of systematic variability in the experimental conditions that accumulate over time. Potential contributors include slow drifts in the detector pose due to wind-induced motion of the aircraft platform, temporal changes in environmental variables, and other subtle experimental dynamics that are negligible on shorter timescales but become significant over several minutes.

In [Fig. 2](#), we also display the spectral templates of all sources considered in the forward model, scaled by the posterior median source strengths and the measurement live times. These scaled templates represent the absolute contributions of the individual sources to the predicted pulse-height spectra. Consistent with the photon emission yields, we observe that the anthropogenic sources  $^{137}\text{Cs}$  and  $^{133}\text{Ba}$  dominate the low-energy range, while the natural terrestrial radionuclides  $\text{K}_{\text{nat}}$ ,  $\text{Th}_{\text{nat}}$ , and  $\text{U}_{\text{nat}}$  dominate at higher energies. The radon source term  $\Delta R_{\text{n,nat}}$  does not significantly contribute to the predicted spectra across all datasets. This observation is corroborated by the posterior results in [Fig. 3](#), which indicate statistically insignificant activity volume concentrations for the radon term. Together, these results confirm that no significant spatiotemporal variations in the radon background occurred between the background and hover flights, supporting the robustness and reliability of the nuisance background correction.

## 2.5 Inferring natural and anthropogenic radionuclide activities

We next evaluate the performance of the Bayesian inversion framework in terms of both precision and accuracy of the inferred radionuclide activities, based on the posterior distributions shown in [Fig. 3](#). Precision is assessed directly from the dispersion of the posterior distributions, whereas accuracy is quantified by comparison with independent reference activities derived from laboratory and *in-situ* gamma-ray assays (see [Section 2.2](#)).

As expected for measurements governed by negative binomial counting statistics, the precision of the posterior estimates for both anthropogenic and natural radionuclide activities generally improves with increasing measurement time. This trend is reflected in the systematic narrowing of the univariate and bivariate posterior marginals shown in [Fig. 3](#), as well as in the overall reduction of credible interval widths reported in Supplementary Tables S3–S4. The observed gain in precision reflects the increased information content of longer acquisitions, even in the presence of overdispersion. Notably, this improvement is not strictly monotonic for all parameters, as elevated overdispersion at longer sampling times can partially offset statistical gains for high-count components. In contrast, the two nuisance parameters,  $\alpha_{\text{NB}}$  and  $\Delta\xi_{\text{Rn,nat}}$ , exhibit posterior dispersions that are largely invariant with respect to measurement time. This behavior indicates intrinsic limits on the information gain for these parameters under the given measurement configurations, consistent with their weak identifiability from the available spectral features.

We assess the accuracy of the inferred activities of the anthropogenic sources  $^{137}\text{Cs}$  and  $^{133}\text{Ba}$  by comparing the posterior median activities with independently measured reference activities obtained from laboratory gamma-ray assays. As shown in [Fig. 3](#), the posterior predictions for the low-count datasets (**Cs\_1s**, **Cs\_5s**, **Ba\_1s**, and **Ba\_5s**) exhibit excellent agreement with the reference values, with relative deviations below 2%. For the high-count datasets (**Cs\_5m**, **Ba\_5m**), the relative deviations increase modestly to  $\sim 5\%$ . This trend is consistent with the elevated overdispersion observed for longer measurement times, as discussed above, which introduces additional variability beyond the Poisson variance limit. Importantly, all deviations remain statistically insignificant within the corresponding credible intervals, demonstrating that the proposed Bayesian framework remains accurate even in the presence of increased overdispersion.

Assessing the accuracy of the inferred activities for the terrestrial primordial radionuclides  $\text{K}_{\text{nat}}$ ,  $\text{Th}_{\text{nat}}$ , and  $\text{U}_{\text{nat}}$  is inherently more challenging, owing to the substantially larger statistical and systematic uncertainties associated with both the posterior estimates and the reference activities obtained from *in-situ* gamma-ray

spectroscopy. These uncertainties arise primarily from spatial heterogeneity in the natural radionuclide distribution and limited counting statistics at higher spectral energies. Nevertheless, for all six datasets, the posterior activity estimates are statistically consistent with the corresponding reference values as well as with each other within their combined uncertainty ranges. This consistency confirms the robustness of the proposed Bayesian framework for quantifying natural background radionuclides under realistic field conditions, despite the reduced accuracy that is fundamentally imposed by the available reference information.

### 3 Discussion

In this work, we have established a full-spectrum Bayesian inference framework that fundamentally advances the quantification of gamma-ray sources in MGRS. By unifying high-fidelity, physics-based numerical template generation with a probabilistically consistent inversion protocol, the proposed methodology directly addresses the two dominant sources of systematic bias identified in current FSA pipelines: inaccurate spectral templates and statistically inconsistent inference under sparse and heterogeneous counting conditions. The resulting framework enables accurate and precise radionuclide quantification from limited acquisition times, while providing robust uncertainty quantification that remains valid across regimes ranging from near-Poisson to pronounced overdispersed statistics.

A central outcome of this study is the demonstrated improvement in quantification accuracy under realistic MGRS conditions. For short acquisitions on the order of seconds—representative of single-pass surveys—the Bayesian inversion achieves agreement with independent laboratory reference activities at the percent level, representing an order-of-magnitude improvement over previously reported FSA-based approaches operating under comparable conditions [41–43]. This gain is not achieved through aggressive regularization or ad hoc constraints, but instead emerges naturally from the combination of physically accurate forward modeling and a likelihood formulation that faithfully reflects the discrete and overdispersed nature of the data. Equally important, the framework delivers robust posterior uncertainties, enabling principled interpretation of inferred activities even in the low-count regime, where conventional methods tend to underestimate uncertainty or yield unstable solutions.

Beyond improved accuracy, the explicit treatment of overdispersion constitutes a key conceptual and practical advance for MGRS. While Poisson-based models implicitly assume static experimental conditions [10, 11, 13], real-world mobile surveys are unavoidably affected by time-dependent variability in platform pose, environmental conditions, and background contributions. The statistically significant increase in inferred overdispersion for longer acquisitions observed in this work provides direct empirical evidence that these effects accumulate over time and significantly influence the count statistics. Importantly, the Bayesian framework allows this variability to be inferred jointly as a nuisance parameter, rather than being neglected through an implicit Poisson assumption and consequently leading to biased source-strength estimates. Because these results were obtained under controlled hover-flight conditions with a fixed source–detector geometry, chosen specifically for reproducibility and validation, the inferred overdispersion levels represent a conservative lower bound. In operational surveys involving dynamic flight paths, heterogeneous terrain, and continuously evolving source–detector configurations, substantially stronger deviations from Poisson statistics are therefore expected. These findings have direct implications for radiological emergency response, environmental monitoring, and nuclear security applications, where biased activity estimates or underestimated uncertainties can lead to incorrect situational assessments. The ability to infer and propagate overdispersion in a principled way is thus a defining advantage of the Bayesian approach in this context.

Building on the results presented here, a number of natural extensions and future directions emerge. First, this work focused on source quantification under a fixed source-identification hypothesis. While this reflects the current operational use of FSA in many MGRS applications, the Bayesian formulation adopted here is

fully compatible with model comparison and hypothesis testing. In particular, integrating MCMC-based evidence estimators [106–108] or nested sampling algorithms [66, 92–96] in the inference pipeline would enable the Bayesian evidence of competing source-composition models to be evaluated and ranked probabilistically. This extension would allow rigorous source identification and discrimination to be performed within the same computational framework used for quantification, eliminating the need for ad hoc decision criteria. Similar evidence-based Bayesian approaches have proven transformative in other inference-driven domains, ranging from cosmology [109–111] to exoplanet research [112, 113], and offer a clear pathway toward unified identification and quantification in MGRS.

Second, our validation focused on terrestrial anthropogenic point sources and natural terrestrial primordial radionuclides distributed in the soil. However, the numerical template-generation strategy introduced here is inherently general. By leveraging high-fidelity Monte Carlo mass models, the framework can accommodate arbitrary gamma-ray source classes and geometries. This includes extended terrestrial anthropogenic sources, atmospheric radon progeny, secondary cosmic-ray–induced emissions, and trace anthropogenic radionuclides in gaseous or aerosol form, among others. As a result, the methodology is directly applicable to a broad spectrum of MGRS scenarios, ranging from airborne environmental surveys and maritime monitoring to planetary surface and orbital missions, without conceptual modification of the inference protocol.

Taken together, these results demonstrate that full-spectrum Bayesian inference, when coupled with physically faithful forward models, overcomes long-standing limitations of MGRS quantification under sparse, heterogeneous, and dynamically evolving measurement conditions. By delivering accurate activity estimates, robust uncertainty quantification, and a principled treatment of overdispersion, this approach provides the methodological and computational foundation for a new generation of MGRS analysis pipelines. Building on this foundation, the framework opens the way to a more statistically rigorous and physics-informed era of mobile gamma-ray spectrometry, enabling reliable decision-making in radiological emergency response, environmental monitoring, nuclear security, and planetary exploration.

## 4 Methods

### 4.1 Spectral template computation

To overcome the prohibitive computational cost of a single-stage brute-force Monte Carlo approach discussed in [Section 2.1](#), we adopt a two-stage template generation strategy. As demonstrated in our previous work [52], this method reduces the evaluation cost to  $\mathcal{O}(1)$ s per template, enabling the rapid generation of high-fidelity spectral template matrices  $\mathbf{M}$ . For completeness, we summarize the main elements of this strategy across this and the following two subsections, with additional details available in Ref. [52].

The spectral response of an MGRS system is determined by the convolution of the differential instrument response function  $d_{E'}R(E', E_\gamma, \Omega', \mathfrak{d})$  with the incident source-strength-normalized double-differential gamma-ray field  $\partial_{E_\gamma}\partial_{\Omega'}\phi_\gamma(E_\gamma, \Omega', \mathfrak{d})$

$$\begin{aligned} \frac{d\psi}{dE'}(E', t) &= \int_0^\infty \int^{4\pi} \frac{dR}{dE'}(E', E_\gamma, \Omega', \mathfrak{d}) \\ &\quad \times \frac{\partial^2\phi_\gamma}{\partial E_\gamma \partial \Omega'}(E_\gamma, \Omega', \mathfrak{d}) d\Omega' dE_\gamma \end{aligned} \quad (3)$$

with  $E'$ ,  $E_\gamma$ ,  $\Omega'$ , and  $\Omega'$  denoting the spectral energy related to the pulse-height in the gamma-ray spectrometer, the energy of the incident gamma ray, the solid angle as well as direction unit vector in the local non-inertial

platform-fixed coordinate system, respectively. For computational evaluation, the integral in [Eq. \(3\)](#) is discretized over spectral energy and direction, allowing us to recast [Eq. \(3\)](#) in matrix notation as

$$\boldsymbol{\Psi}(\mathfrak{d}) \approx \sum_{k=1}^{N_{\Omega'}} \mathbf{R}(\boldsymbol{\Omega}'_k, \mathfrak{d}) \boldsymbol{\Phi}_{\gamma}(\boldsymbol{\Omega}'_k, \mathfrak{d}) \quad (4)$$

where  $\boldsymbol{\Psi} \in \mathbb{R}_+^{N_y}$  denotes the spectral template vector introduced in [Section 2.1](#),  $\mathbf{R} \in \mathbb{R}_{\geq 0}^{N_y \times N_{E_{\gamma}}}$  the instrument response matrix, and  $\boldsymbol{\Phi}_{\gamma} \in \mathbb{R}_{\geq 0}^{N_{E_{\gamma}}}$  the gamma-ray flux vector. The individual elements of the instrument response matrix are estimated by scaling the differential instrument response components with the corresponding spectral energy bin width, i.e.,  $R(E'_i, E_{\gamma,j}, \boldsymbol{\Omega}'_k, \mathfrak{d}) \approx d_{E'} R(E'_i, E_{\gamma,j}, \boldsymbol{\Omega}'_k, \mathfrak{d}) \Delta E'_i$ . Similarly, we compute the individual elements of the gamma-ray flux vector by scaling the double-differential gamma-ray flux components with the corresponding energy and solid angle bin widths, i.e.,  $\phi_{\gamma}(E_{\gamma,j}, \boldsymbol{\Omega}'_k, \mathfrak{d}) \approx \partial_{E_{\gamma}} \partial_{\Omega'} \phi_{\gamma}(E_{\gamma,j}, \boldsymbol{\Omega}'_k, \mathfrak{d}) \Delta E_{\gamma,j} \Delta \Omega'_k$ .

To compute the spectral templates  $\boldsymbol{\Psi}$  as defined in [Eq. \(4\)](#), we implemented the convolution using the `pagetimes` routine in **MATLAB®** (Version R2024a), which enables efficient multithreaded evaluation of the directional matrix–vector products. Prior to convolution, the IRF and flux banks must be interpolated onto a common discretization scheme. Spectral alignment is achieved by interpolating the IRF onto the regular energy grid of the gamma-ray flux simulation [114], while angular alignment is handled by azimuthal expansion in 30° steps followed by mapping to the local platform-fixed frame using Tait–Bryan rotations, that define the platform’s instantaneous attitude relative to the global frame. The aligned quantities are then convolved to produce the spectral templates, with statistical and systematic uncertainties propagated through the pipeline. On a standard workstation (8 cores, 2.1 GHz), the total runtime for template generation including uncertainty estimation is  $\mathcal{O}(1)$  s per template. In the next subsections, we detail the generation of both the instrument response matrix as well as the gamma-ray flux vector banks for the benchmark study discussed in [Sections 2.2 to 2.5](#).

## 4.2 Instrument response function

The instrument response matrices were estimated using high-fidelity Monte Carlo radiation transport simulations of the well validated SAGRS mass model [51]. Following established practices for spaceborne gamma-ray spectrometers [23, 25–27], we illuminated the system with circular monoenergetic plane waves over a grid of gamma-ray energies and incident directions in the platform-fixed coordinate system. The IRF elements were derived as the normalized spectral counts in each pulse-height channel, with source radii chosen to ensure invariance of the response (see Ref. [52]). The simulation grid spanned 30 energies between 50 keV and 3 MeV combined with 134 incident directions, yielding 4020 runs. To account for temporal variability of the platform, we generated IRFs for eight distinct mass-model states defined by fuel load, crew occupancy, and landing gear position, including those states encountered during the survey described in [Section 2.2](#). Each simulation tracked  $10^7$  primary histories using **FLUKA** (v4-2.2) [62, 100, 101] with the `precisio` physics settings, providing coupled photon-electron-positron transport, secondary particle production, and X-ray fluorescence. To reproduce the nonproportional scintillation response of the SAGRS system, a dedicated scintillation model calibrated in prior work [51, 115] was implemented through `comscw` and `usrglo`. Motivated by the range of the transported particles, transport thresholds were set to 1 keV in the detector volume and 10 keV elsewhere. Energy deposition events were recorded per crystal using custom `usreou` routines and reduced to expected pulse-height spectra with the **NPScinMC** pipeline [51]. Due to the substantial computational cost of these Monte Carlo simulations, we employed high-performance computing infrastructure available at the Paul Scherrer Institute (2.6 GHz nominal clock speed). Generating the complete set of IRFs required  $\sim 5.5 \times 10^4$  core-hours.

### 4.3 Gamma-ray flux bank

We generated double-differential gamma-ray flux banks for all sources included in the forward models (see [Section 2.3](#)) using the **FLUKA** code (v4-2.2) [62, 100, 101] on HPC infrastructure. Specifically, we adopted the built-in **USRYIELD** method to score the double-differential flux with a bin width of 0.5 keV for the gamma-ray energy  $E_\gamma$  and 5° for the polar angle  $\theta$  in a global inertial coordinate system (exploiting azimuthal invariance). Similar to the IRF generation, we adopted the **precisio** physics settings with a 10 keV transport threshold. The accumulated computation time was  $\sim 10^2$  core-hours per source, with  $2 \times 10^9$  primaries distributed across  $10^2$  independent runs.

For all flux simulations, we adopted a dynamic environmental mass model with three main mass elements, i.e., the atmosphere, the terrestrial soil, as well as paved surfaces present at the training ground. These components were modeled as homogeneous media with compositional data sourced from Ref. [116]. The atmosphere was modeled for each measurement separately as homogeneous humid air as a function of the recorded air temperature, pressure, and humidity (see [Supplementary Table S1](#)). Motivated by the mean free path of the primary photons in air, atmospheric boundaries were confined to a 3 km radius sphere, centered at the SAGRS location. The ground was limited to a vertical extension of 10 m. In addition to the environmental media, we included also detailed mass models of the deployed radionuclide sources and custom source holders (see Ref. [51]).

Radionuclide emissions were simulated with the **FLUKA raddecay** module in semi-analogue mode, according to related decay schemes. Anthropogenic source volumes were explicitly modeled, with source strengths  $\xi_{\text{Ba-133}}$  and  $\xi_{\text{Cs-137}}$  parameterized by the absolute source activity in Bq. For the natural terrestrial radionuclides ( $K_{\text{nat}}$ ,  $\text{Th}_{\text{nat}}$ ,  $U_{\text{nat}}$ ), we assumed secular equilibrium with progeny and a spatially uniform distribution within the soil. Corresponding source strengths ( $\xi_{K\text{-nat}}$ ,  $\xi_{Th\text{-nat}}$ ,  $\xi_{U\text{-nat}}$ ) were parameterized by the activity mass concentration in  $\text{Bq kg}^{-1}$ . Similarly, the atmospheric radon source term discussed in [Section 2.3](#) was implemented as a homogeneous atmospheric  $^{222}_{86}\text{Rn}$  volume source in secular equilibrium with its progeny up to but excluding  $^{210}_{82}\text{Pb}$ , and with the source strength  $\Delta\xi_{\text{Rn-nat}}$  expressed as activity volume concentration in  $\text{Bq m}^{-3}$ .

### 4.4 Swiss Airborne Gamma-Ray Spectrometry System

The Swiss Airborne Gamma-Ray Spectrometry (SAGRS) system is a helicopter-borne MGRS platform jointly operated by the National Emergency Operations Centre (NEOC), the Nuclear Biological Chemical defence and Explosive Ordnance Disposal Centre of Excellence (NBC-EOD), and the Swiss Air Force for environmental surveys and emergency response. The system is fully deployable and airborne within four hours, enabling rapid and flexible operations under a wide range of survey and emergency scenarios. A brief technical summary is provided below. Comprehensive specifications and validation studies are reported in Refs. [51, 52, 97].

The detector assembly consists of four prismatic NaI(Tl) scintillation crystals (Saint-Gobain 4×4H16/3.5-X), each measuring 10.2 cm × 10.2 cm × 40.6 cm. The crystals are individually enclosed in aluminum housings, optically coupled to Hamamatsu R10755 photomultiplier tubes, and equipped with dedicated readout electronics. They are embedded in thermally insulating, vibration-damping polyethylene foam and mounted in a rugged aluminum box (outer dimensions 90 cm × 64 cm × 35 cm). The unit is installed in the cargo bay of an Aérospatiale AS332M1 Super Puma helicopter, aligned with the fuselage underside to maximize sensitivity to terrestrial radiation. System integration includes avionics via an ARINC 429 bus. Recorded parameters comprise global navigation satellite system position, radar altitude, helicopter orientation, and fuel state. These auxiliary measurements are synchronized with the spectrometer data and serve as input to the forward model.

Spectral acquisition is performed in bin mode at 1 Hz, with individual spectra recorded for each of the four scintillator assemblies, alongside a combined sum spectrum representing the aggregated detector response. Each spectrum comprises 1024 channels spanning  $\sim 30$  keV to  $\sim 3.072$  MeV. The readout electronics provide automatic gain stabilization, linearization with offset correction, and live-time tracking. Survey operations are controlled

via two onboard operator stations interfaced to a central data server, with the full system, including support hardware, having a total mass of  $\sim 290$  kg.

#### 4.5 Bayesian computation

Following the Bayesian framework outlined in [Section 2.1](#), we adopt a negative binomial probabilistic forward model to describe the observed counts  $C \in \mathbb{N}$  in the set of recorded pulse-height spectra  $\mathcal{Y}$ , accounting for both measurement uncertainty and overdispersion arising from the experimental process (see [Section 2.3](#)). The associated likelihood in [Eq. \(2\)](#) is formulated using a parameterization established in prior studies [103, 104, 117], with the dispersion parameter  $\alpha_{\text{NB}} \in \mathbb{R}_+$  governing overdispersion in the observed counts:

$$\mathcal{L}(\boldsymbol{\theta}; \mathcal{Y}, \mathcal{D}) = \prod_{k=1}^{N_{\mathcal{Y}}} \prod_{j=1}^{N_y} \frac{\Gamma(C_{k,j} + \frac{1}{\alpha_{\text{NB}}})}{\Gamma(\frac{1}{\alpha_{\text{NB}}}) \Gamma(C_{k,j} + 1)} \left( \frac{1}{1 + \alpha_{\text{NB}} \mathcal{M}(\boldsymbol{\xi}, \mathbf{d}_k)} \right)^{\frac{1}{\alpha_{\text{NB}}}} \left( \frac{1}{1 + [\alpha_{\text{NB}} \mathcal{M}(\boldsymbol{\xi}, \mathbf{d}_k)]^{-1}} \right)^{C_{k,j}}. \quad (5)$$

Here,  $\Gamma(\cdot)$  denotes the gamma function and  $\mathcal{M}(\cdot)$  the deterministic forward operator introduced in [Eq. \(1\)](#), mapping source strengths  $\boldsymbol{\xi}$  and experimental conditions  $\mathbf{d}_k$  to expected counts. The observed counts  $C_{k,j}$  correspond to pulse-height channel  $j$  in spectrum  $k$ . In this work, each inverse problem outlined in [Section 2.3](#) is solved independently. Thus, the spectral dataset  $\mathcal{Y}$  and associated condition set  $\mathcal{D}$  reduce to mutually exclusive singletons ( $N_{\mathcal{Y}} = 1$ ). This formulation enables rigorous Bayesian inference over  $\boldsymbol{\theta} := (\boldsymbol{\xi}, \alpha_{\text{NB}})$ , capturing both measurement uncertainty and overdispersion in the observed data. It is worth adding that, because the gamma function terms in [Eq. \(5\)](#) grow rapidly for moderately large arguments, special care is required when numerically evaluating the likelihood. To avoid under- or overflow, it is advisable to operate with the logarithm of the likelihood function, known as the log-likelihood, instead of directly evaluating [Eq. \(5\)](#):

$$\begin{aligned} \log \mathcal{L}(\boldsymbol{\theta}; \mathcal{Y}, \mathcal{D}) = & \sum_{k=1}^{N_{\mathcal{Y}}} \sum_{j=1}^{N_y} \log \Gamma\left(C_{k,j} + \frac{1}{\alpha_{\text{NB}}}\right) - \log \Gamma\left(\frac{1}{\alpha_{\text{NB}}}\right) \\ & - \log \Gamma(C_{k,j} + 1) - \frac{1}{\alpha_{\text{NB}}} \log (1 + \alpha_{\text{NB}} \mathcal{M}(\boldsymbol{\xi}, \mathbf{d}_k)) \\ & - C_{k,j} \log \left(1 + \frac{1}{\alpha_{\text{NB}} \mathcal{M}(\boldsymbol{\xi}, \mathbf{d}_k)}\right) \end{aligned} \quad (6)$$

with numerically stable implementations of the log-gamma function  $\log \Gamma(\cdot)$  being readily available in all major scientific computing environments, including **Python**, **MATLAB**<sup>®</sup>, and **C++**.

The likelihood specification in [Eq. \(5\)](#) forms the first element of the Bayesian framework. Completing the posterior model in [Eq. \(2\)](#) requires assigning suitable priors to the model parameters  $\boldsymbol{\theta}$ . To avoid overly restrictive assumptions on these prior distributions, we adopted weakly informative, statistically independent marginal priors  $\pi(\boldsymbol{\theta}) := \prod_{i=1}^{N_{\xi}+1} \pi(\theta_i)$  for all model parameters  $\theta$ , with the marginal priors  $\pi(\theta)$  defined based on the principle of maximum entropy [118]. A full list of all marginal prior distributions is provided in Supplementary Table S2.

All Bayesian computations were performed with the **UQLab** code [64] using an affine invariant ensemble MCMC algorithm [91] to sample the posterior distribution  $\pi(\boldsymbol{\theta} | \mathcal{Y}, \mathcal{D}, \mathcal{F})$  in [Eq. \(2\)](#) via Bayes' theorem. The MCMC algorithm was executed with 24 parallel chains, each running  $5 \times 10^3$  iterations. The burn-in phase was set to 20% resulting in a total of  $9.6 \times 10^4$  posterior samples. The convergence and precision of the MCMC

simulations were carefully assessed using standard diagnostics tools [70, 119], showing a potential scale reduction factor  $\hat{R} < 1.02$  and effective sample size  $\text{ESS} > 400$  across all MCMC runs. Additional trace and convergence plots for the individual parameters  $\theta$  and point estimators (Supplementary Figs. S2–S6) alongside a full list of the Bayesian inversion results (Supplementary Tables S3 and S4) can be found in the Supplementary Information File for this study.

**Data availability.** All experimental data presented herein have been deposited in the Zenodo repository under accession code <https://doi.org/10.5281/zenodo.18004441> [120].

**Code availability.** The FLUKA code [62] used for Monte Carlo radiation transport and detector response simulations is available at <https://fluka.cern/>. We adopted the graphical user interphase FLAIR [102], available at <https://flair.web.cern.ch/flair/>, to setup the FLUKA input files and create the mass model figures. The custom FLUKA user routines adopted in the Monte Carlo simulations have been deposited on the ETH Research Collection repository under accession code <https://doi.org/10.3929/ethz-b-000595727> [121]. Data processing, Bayesian inference computation and figure creation was performed by the MATLAB<sup>®</sup> code in combination with the open-source toolbox UQLab [64] available at <https://www.uqlab.com/>.

## References

- [1] Jones, D. G. Development and application of marine gamma-ray measurements: A review. *J. Environ. Radioact.* **53**, 313–333 (2001).
- [2] Lee, M. S. *et al.* Real-time wireless marine radioactivity monitoring system using a SiPM-based mobile gamma spectroscopy mounted on an unmanned marine vehicle. *Nucl. Eng. Technol.* **55**, 2158–2165 (2023).
- [3] Rosenthal, J. J., de Almeidat, C. E. & Mendonca, A. H. The Radiological Accident in Goiania. *Health Phys.* **60**, 7–15 (1991).
- [4] Drovnikov, V. V., Egorov, N. Y., Kovalenko, V. V., Serboulov, Y. A. & Zadorozhny, Y. A. Some results of the airborne high energy resolution gamma-spectrometry application for the research of the USSR European territory radioactive contamination in 1986 caused by the Chernobyl accident. *J. Environ. Radioact.* **37**, 223–234 (1997).
- [5] Lyons, C. & Colton, D. Aerial Measuring System in Japan. *Health Phys.* **102**, 509 (2012).
- [6] Torii, T., Sugita, T., Okada, C. E., Reed, M. S. & Blumenthal, D. J. Enhanced Analysis Methods to Derive the Spatial Distribution of  $^{131}\text{I}$  Deposition on the Ground by Airborne Surveys at an Early Stage after the Fukushima Daiichi Nuclear Power Plant Accident. *Health Phys.* **105**, 192–200 (2013).
- [7] Sanada, Y., Sugita, T., Nishizawa, Y., Kondo, A. & Torii, T. The aerial radiation monitoring in Japan after the Fukushima Daiichi nuclear power plant accident. *Nucl. Sci. Technol.* **4**, 76–80 (2014).
- [8] Deal, L. J., Doyle, J. F., Burson, Z. G. & Boyns, P. K. Locating the lost athena missile in mexico by the aerial radiological measuring system (ARMS). *Health Phys.* **23**, 95–98 (1972).
- [9] Prieto, E., Jabaloyas, E., Casanovas, R., Rovira, C. & Salvadó, M. Set up of a gamma spectrometry mobile unit equipped with  $\text{LaBr}_3(\text{Ce})$  detectors for radioactivity monitoring. *Radiat. Phys. Chem.* **168**, 108600 (2020).

- [10] Hellfeld, D. *et al.* Free-moving Quantitative Gamma-ray Imaging. *Sci. Rep.* **11**, 20515 (2021).
- [11] Bandstra, M. S. *et al.* Improved Gamma-Ray Point Source Quantification in Three Dimensions by Modeling Attenuation in the Scene. *IEEE Trans. Nucl. Sci.* **68**, 2637–2646 (2021).
- [12] Curtis, J. C. *et al.* Simulation and validation of the Mobile Urban Radiation Search (MURS) gamma-ray detector response. *Nucl. Instrum. Methods Phys. Res. Sect. Accel. Spectrometers Detect. Assoc. Equip.* **954**, 161128 (2020).
- [13] Salathe, M. *et al.* Determining urban material activities with a vehicle-based multi-sensor system. *Phys. Rev. Res.* **3**, 023070 (2021).
- [14] Fishman, G. J. *et al.* Discovery of Intense Gamma-Ray Flashes of Atmospheric Origin. *Science* **264**, 1313–1316 (1994).
- [15] Briggs, M. S. *et al.* First results on terrestrial gamma ray flashes from the Fermi Gamma-ray Burst Monitor. *J. Geophys. Res. Space Phys.* **115** (2010).
- [16] Tavani, M. *et al.* Terrestrial Gamma-Ray Flashes as Powerful Particle Accelerators. *Phys. Rev. Lett.* **106**, 018501 (2011).
- [17] Smith, D. M. *et al.* A terrestrial gamma ray flash observed from an aircraft. *J. Geophys. Res. Atmospheres* **116**, 20124 (2011).
- [18] Gjesteland, T. *et al.* Observation of intrinsically bright terrestrial gamma ray flashes from the Mediterranean basin. *J. Geophys. Res. Atmospheres* **120**, 12,143–12,156 (2015).
- [19] Neubert, T. *et al.* A terrestrial gamma-ray flash and ionospheric ultraviolet emissions powered by lightning. *Science* **367**, 183–186 (2020).
- [20] Appleton, J. D., Miles, J. C., Green, B. M. & Larmour, R. Pilot study of the application of Tellus airborne radiometric and soil geochemical data for radon mapping. *J. Environ. Radioact.* **99**, 1687–1697 (2008).
- [21] Sinclair, L. E. *et al.* Aerial measurement of radioxenon concentration off the west coast of vancouver island following the fukushima reactor accident. *J. Environ. Radioact.* **102**, 1018–1023 (2011).
- [22] Baldoncini, M. *et al.* Exploring atmospheric radon with airborne gamma-ray spectroscopy. *Atmos. Environ.* **170**, 259–268 (2017).
- [23] Prettyman, T. H. *et al.* Elemental composition of the lunar surface: Analysis of gamma ray spectroscopy data from Lunar Prospector. *J. Geophys. Res. Planets* **111** (2006).
- [24] Hahn, B. C. *et al.* Mars Odyssey Gamma Ray Spectrometer elemental abundances and apparent relative surface age: Implications for Martian crustal evolution. *J. Geophys. Res. Planets* **112** (2007).
- [25] Kobayashi, S. *et al.* Determining the absolute abundances of natural radioactive elements on the lunar surface by the kaguya gamma-ray spectrometer. *Space Sci. Rev.* **154**, 193–218 (2010).
- [26] Prettyman, T. H. *et al.* Dawn’s gamma ray and neutron detector. *Space Sci. Rev.* **163**, 371–459 (2011).

[27] Peplowski, P. N. *et al.* Radioactive elements on Mercury's surface from MESSENGER: Implications for the planet's formation and evolution. *Science* **333**, 1850–1852 (2011).

[28] Peplowski, P. N. The global elemental composition of 433 Eros: First results from the NEAR gamma-ray spectrometer orbital dataset. *Planet. Space Sci.* **134**, 36–51 (2016).

[29] Prettyman, T. H. *et al.* Extensive water ice within Ceres' aqueously altered regolith: Evidence from nuclear spectroscopy. *Science* **355**, 55–59 (2017).

[30] Prettyman, T. H. *et al.* Elemental composition and mineralogy of Vesta and Ceres: Distribution and origins of hydrogen-bearing species. *Icarus* **318**, 42–55 (2019).

[31] Sanada, Y. & Torii, T. Aerial radiation monitoring around the Fukushima Dai-ichi nuclear power plant using an unmanned helicopter. *J. Environ. Radioact.* **139**, 294–299 (2015).

[32] Nishizawa, Y., Yoshida, M., Sanada, Y. & Torii, T. Distribution of the  $^{134}\text{Cs}/^{137}\text{Cs}$  ratio around the Fukushima Daiichi nuclear power plant using an unmanned helicopter radiation monitoring system. *J. Nucl. Sci. Technol.* **53**, 468–474 (2016).

[33] Connor, D., Martin, P. G. & Scott, T. B. Airborne radiation mapping: Overview and application of current and future aerial systems. *Int. J. Remote Sens.* **37**, 5953–5987 (2016).

[34] Naumenko, A. *et al.* Autonomous NaI(Tl) gamma-ray spectrometer for in situ underwater measurements. *Nuclear Instruments and Methods in Physics Research Section A: Accelerators, Spectrometers, Detectors and Associated Equipment* **908**, 97–109 (2018).

[35] Pradeep Kumar, K. A., Shanmuga Sundaram, G. A., Sharma, B. K., Venkatesh, S. & Thiruvengadathan, R. Advances in gamma radiation detection systems for emergency radiation monitoring. *Nucl. Eng. Technol.* **52**, 2151–2161 (2020).

[36] Grasty, R. L., Glynn, J. E. & Grant, J. A. The analysis of multichannel airborne gamma-ray spectra. *GEOPHYSICS* **50**, 2611–2620 (1985).

[37] Minty, B. R., McFadden, P. & Kennett, B. L. Multichannel processing for airborne gamma-ray spectrometry. *Geophysics* **63**, 1971–1985 (1998).

[38] Hendriks, P. H., Limburg, J. & De Meijer, R. J. Full-spectrum analysis of natural  $\gamma$ -ray spectra. *J. Environ. Radioact.* **53**, 365–380 (2001).

[39] Baré, J. & Tondeur, F. Gamma spectrum unfolding for a NaI monitor of radioactivity in aquatic systems: Experimental evaluations of the minimal detectable activity. *Appl. Radiat. Isot.* **69**, 1121–1124 (2011).

[40] Caciolli, A. *et al.* A new FSA approach for in situ  $\gamma$  ray spectroscopy. *Sci. Total Environ.* **414**, 639–645 (2012).

[41] Ohera, M., Gryc, L., Nováková, M., Češpírová, I. & Sas, D. Application of unmanned aerial vehicles in emergency radiation monitoring. *Radiation Measurements* **174**, 107111 (2024).

[42] Sinclair, L. E. *et al.* Aerial Mobile Radiation Survey Following Detonation of a Radiological Dispersal Device. *Health Phys.* **110**, 458–470 (2016).

[43] Butterweck, G. *et al.* Aeroradiometric measurements in the framework of the Swiss exercise ARM23. Tech. Rep., Paul Scherrer Institut (PSI), Villigen PSI, Switzerland (2024).

[44] Dickson, B. H., Bailey, R. C. & Grasty, R. L. Utilizing multi-channel airborne gamma-ray spectra. *Can. J. Earth Sci.* **18**, 1793–1801 (1981).

[45] Grasty, R. L., Holman, P. B. & Blanchard, Y. B. Transportable calibration pads for ground and airborne gamma-ray spectrometers. *Geol. Surv. Can.* **90** (1991).

[46] Minty, B. R. S., Morse, M. P. & Richardson, L. M. Portable Calibration Sources For Airborne Gamma-ray Spectrometers. *Explor. Geophys.* **21**, 187–195 (1990).

[47] Allyson, J. D. & Sanderson, D. C. Monte Carlo simulation of environmental airborne gamma-spectrometry. *J. Environ. Radioact.* **38**, 259–282 (1998).

[48] Billings, S. & Hovgaard, J. Modeling detector response in airborne gamma-ray spectrometry. *Geophysics* **64**, 1378–1392 (1999).

[49] Zhang, Q. *et al.* A hybrid method on sourceless sensitivity calculation for airborne gamma-ray spectrometer. *Appl. Radiat. Isot.* **137**, 68–72 (2018).

[50] Kulisek, J. A. *et al.* A 3D simulation look-up library for real-time airborne gamma-ray spectroscopy. *Nucl. Instrum. Methods Phys. Res. Sect. Accel. Spectrometers Detect. Assoc. Equip.* **879**, 84–91 (2018).

[51] Breitenmoser, D., Stabilini, A., Kasprzak, M. M. & Mayer, S. Development and validation of a high-fidelity full-spectrum Monte Carlo model for the Swiss airborne gamma-ray spectrometry system. *Nuclear Instruments and Methods in Physics Research Section A: Accelerators, Spectrometers, Detectors and Associated Equipment* **1077**, 170512 (2025).

[52] Breitenmoser, D., Stabilini, A. & Mayer, S. Full-spectrum modeling of mobile gamma-ray spectrometry systems in scattering media (2025). [arXiv:2506.17820](https://arxiv.org/abs/2506.17820).

[53] Minty, B. R. Airborne gamma-ray spectrometric background estimation using full spectrum analysis. *Geophysics* **57**, 279–287 (1992).

[54] Crossley, D. J. & Reid, A. B. Inversion of gamma-ray data for element abundances. *GEOPHYSICS* **47**, 117–126 (1982).

[55] Minty, B. R. S. & Kennett, B. L. N. Optimum Channel Combinations for Multichannel Airborne Gamma-Ray Spectrometry. *Explor. Geophys.* **26**, 292–301 (1995).

[56] Humphrey, P. J., Liu, W. & Buote, D. A.  $\chi^2$  AND POISSONIAN DATA: BIASES EVEN IN THE HIGH-COUNT REGIME AND HOW TO AVOID THEM. *ApJ* **693**, 822 (2009).

[57] Yamada, S. *et al.* Poisson vs. Gaussian statistics for sparse X-ray data: Application to the soft X-ray spectrometer. *Publ Astron Soc Jpn Nihon Tenmon Gakkai* **71**, 75 (2019).

[58] Tak, H. *et al.* Six Maxims of Statistical Acumen for Astronomical Data Analysis. *ApJS* **275**, 30 (2024).

[59] Romano, P. K. *et al.* OpenMC: A state-of-the-art Monte Carlo code for research and development. *Annals of Nuclear Energy* **82**, 90–97 (2015).

[60] Allison, J. *et al.* Recent developments in Geant4. *Nucl. Instrum. Methods Phys. Res. A* **835**, 186–225 (2016).

[61] Goorley, T. *et al.* Features of MCNP6. *Annals of Nuclear Energy* **87**, 772–783 (2016).

[62] Ahdida, C. *et al.* New Capabilities of the FLUKA Multi-Purpose Code. *Front. Phys.* **9**, 788253 (2022).

[63] Sato, T. *et al.* Recent improvements of the particle and heavy ion transport code system – PHITS version 3.33. *J. Nucl. Sci. Technol.* **61**, 127–135 (2024).

[64] Marelli, S. & Sudret, B. UQLab: A Framework for Uncertainty Quantification in Matlab. *ICVRAM* 2554–2563 (2014).

[65] Carpenter, B. *et al.* Stan: A Probabilistic Programming Language. *J. Stat. Softw.* **76**, 1–32 (2017).

[66] Buchner, J. UltraNest - a robust, general purpose Bayesian inference engine. *J. Open Source Softw.* **6**, 3001 (2021).

[67] Abril-Pla, O. *et al.* PyMC: A modern, and comprehensive probabilistic programming framework in Python. *PeerJ Comput. Sci.* **9**, e1516 (2023).

[68] Kennedy, M. C. & O'Hagan, A. Bayesian calibration of computer models. *J. R. Stat. Soc. Ser. B Stat. Methodol.* **63**, 425–464 (2001).

[69] Trotta, R. Bayes in the sky: Bayesian inference and model selection in cosmology. *Contemp. Phys.* **49**, 71–104 (2008).

[70] Gelman, A. *et al.* *Bayesian Data Analysis* 3rd edn (Chapman and Hall/CRC, New York, USA, 2013).

[71] von Toussaint, U. Bayesian inference in physics. *Rev. Mod. Phys.* **83**, 943–999 (2011).

[72] D'Agostini, G. Bayesian inference in processing experimental data: Principles and basic applications. *Rep. Prog. Phys.* **66**, 1383 (2003).

[73] Andreon, S. & Weaver, B. *Bayesian Methods for the Physical Sciences: Learning from Examples in Astronomy and Physics* Vol. 4 of *Springer Series in Astrostatistics* (Springer International Publishing, Cham, 2015).

[74] Yuen, K.-V. *Bayesian Methods for Structural Dynamics and Civil Engineering* (John Wiley & Sons, 2010).

[75] Nichols, J. M. & Murphy, K. D. *Modeling and Estimation of Structural Damage* (John Wiley & Sons, 2016).

[76] Diggle, P. J., Tawn, J. A. & Moyeed, R. A. Model-based geostatistics. *J. R. Stat. Soc. Ser. C Appl. Stat.* **47**, 299–350 (2002).

[77] Bennett, A. F. *Inverse Modeling of the Ocean and Atmosphere* (Cambridge University Press, Cambridge, 2002).

[78] Drummond, A. J. & Bouckaert, R. R. *Bayesian Evolutionary Analysis with BEAST* (Cambridge University Press, Cambridge, 2015).

[79] Broemeling, L. D. *Bayesian Biostatistics and Diagnostic Medicine* (Chapman and Hall/CRC, New York, 2007).

[80] Murphy, K. P. *Machine Learning: A Probabilistic Perspective* (MIT press, 2012).

[81] Russell, S. J. & Norvig, P. *Artificial Intelligence: A Modern Approach* 4 edn (Pearson, 2020).

[82] Bishop, C. M. *Pattern Recognition and Machine Learning* (Springer, New York, 2006).

[83] Jackman, S. *Bayesian Analysis for the Social Sciences* (John Wiley & Sons, 2009).

[84] Gill, J. *Bayesian Methods: A Social and Behavioral Sciences Approach, Third Edition* 3 edn (Chapman and Hall/CRC, New York, 2015).

[85] Paradis, H. *et al.* Spectral unmixing applied to fast identification of  $\gamma$ -emitting radionuclides using NaI(Tl) detectors. *Appl. Radiat. Isot.* **158**, 109068 (2020).

[86] André, R., Bobin, C., Bobin, J., Xu, J. & de Vismes Ott, A. Metrological approach of  $\gamma$ -emitting radionuclides identification at low statistics: Application of sparse spectral unmixing to scintillation detectors. *Metrologia* **58**, 15011–15025 (2021).

[87] Metropolis, N., Rosenbluth, A. W., Rosenbluth, M. N., Teller, A. H. & Teller, E. Equation of State Calculations by Fast Computing Machines. *The Journal of Chemical Physics* **21**, 1087–1092 (1953).

[88] Hastings, W. K. Monte Carlo sampling methods using Markov chains and their applications. *Biometrika* **57**, 97–109 (1970).

[89] Duane, S., Kennedy, A. D., Pendleton, B. J. & Roweth, D. Hybrid Monte Carlo. *Physics Letters B* **195**, 216–222 (1987).

[90] Foreman-Mackey, D., Hogg, D. W., Lang, D. & Goodman, J. Emcee : The MCMC Hammer. *Publ. Astron. Soc. Pac.* **125**, 306–312 (2013).

[91] Goodman, J. & Weare, J. Ensemble samplers with affine invariance. *Commun. Appl. Math. Comput. Sci.* **5**, 65–80 (2010).

[92] Skilling, J. Nested Sampling. *AIP Conf. Proc.* **735**, 405 (2004).

[93] Feroz, F., Hobson, M. P. & Bridges, M. MultiNest: An efficient and robust Bayesian inference tool for cosmology and particle physics. *Mon. Not. R. Astron. Soc.* **398**, 1601–1614 (2009).

[94] Handley, W. J., Hobson, M. P. & Lasenby, A. N. Polychord: Next-generation nested sampling. *Mon. Not. R. Astron. Soc.* **453**, 4384–4398 (2015).

[95] Speagle, J. S. DYNESTY: A dynamic nested sampling package for estimating Bayesian posteriors and evidences. *Mon. Not. R. Astron. Soc.* **493**, 3132–3158 (2020).

[96] Ashton, G. *et al.* Nested sampling for physical scientists. *Nat. Rev. Methods Primer* **2022** *21* **2**, 1–22 (2022).

[97] Breitenmoser, D., Butterweck, G., Kasprzak, M. M., Yukihara, E. G. & Mayer, S. Experimental and Simulated Spectral Gamma-Ray Response of a NaI(Tl) Scintillation Detector used in Airborne Gamma-Ray Spectrometry. *Adv. Geosci.* **57**, 89–107 (2022).

[98] Butterweck, G. *et al.* Aeroradiometric measurements in the framework of the Swiss Exercise ARM22. Tech. Rep., Paul Scherrer Institut (PSI), Villigen PSI, Switzerland (2023).

[99] Butterweck, G. *et al.* Aeroradiometric measurements in the framework of the Swiss exercise ARM20. Tech. Rep., Paul Scherrer Institut (PSI), Villigen PSI, Switzerland (2021).

[100] Böhlen, T. T. *et al.* The FLUKA Code: Developments and challenges for high energy and medical applications. *Nucl. Data Sheets* **120**, 211–214 (2014).

[101] Battistoni, G. *et al.* Overview of the FLUKA code. *Ann. Nucl. Energy* **82**, 10–18 (2015).

[102] Vlachoudis, V. Flair: A powerful but user friendly graphical interface for FLUKA. *Int. Conf. Math. Comput. Methods React. Phys. MC 2009* (2009).

[103] Hünnefeld, M. *et al.* Combining Maximum-Likelihood with Deep Learning for Event Reconstruction in IceCube. *Proc. Sci.* **395**, 1065 (2022).

[104] Salinas, D., Flunkert, V., Gasthaus, J. & Januschowski, T. DeepAR: Probabilistic forecasting with autoregressive recurrent networks. *Int. J. Forecast.* **36**, 1181–1191 (2020).

[105] Santarelli, M. F., Positano, V. & Landini, L. Measured PET Data Characterization with the Negative Binomial Distribution Model. *J. Med. Biol. Eng.* **37**, 299–312 (2017).

[106] Perrakis, K., Ntzoufras, I. & Tsionas, E. G. On the use of marginal posteriors in marginal likelihood estimation via importance sampling. *Computational Statistics & Data Analysis* **77**, 54–69 (2014).

[107] Metodiev, M. *et al.* Easily Computed Marginal Likelihoods from Posterior Simulation Using the THAMES Estimator. *Bayesian Anal.* **-1**, 1–28 (2024).

[108] Llorente, F., Martino, L., Delgado, D. & López-Santiago, J. Marginal Likelihood Computation for Model Selection and Hypothesis Testing: An Extensive Review. *SIAM Rev.* **65**, 3–58 (2023).

[109] Veitch, J. Parameter estimation for compact binaries with ground-based gravitational-wave observations using the LALInference software library. *Phys. Rev. D* **91** (2015).

[110] Ashton, G. *et al.* Bilby: A User-friendly Bayesian Inference Library for Gravitational-wave Astronomy. *ApJS* **241**, 27 (2019).

- [111] Smith, R. J. E., Ashton, G., Vajpeyi, A. & Talbot, C. Massively parallel Bayesian inference for transient gravitational-wave astronomy. *MNRAS* **498**, 4492–4502 (2020).
- [112] MacDonald, R. J. & Madhusudhan, N. HD 209458b in new light: Evidence of nitrogen chemistry, patchy clouds and sub-solar water. *MNRAS* **469**, 1979–1996 (2017).
- [113] Pinhas, A., Rackham, B. V., Madhusudhan, N. & Apai, D. Retrieval of planetary and stellar properties in transmission spectroscopy with Aura. *MNRAS* **480**, 5314–5331 (2018).
- [114] Jandel, M. *et al.* Decomposition of continuum  $\gamma$ -ray spectra using synthesized response matrix. *Nucl. Instrum. Methods Phys. Res. Sect. Accel. Spectrometers Detect. Assoc. Equip.* **516**, 172–183 (2004).
- [115] Breitenmoser, D., Cerutti, F., Butterweck, G., Kasprzak, M. M. & Mayer, S. Emulator-based Bayesian inference on non-proportional scintillation models by compton-edge probing. *Nat. Commun.* **14**, 7790 (2023).
- [116] McConn, R. J., Gesh, C. J., Pagh, R. T. & Rucker, R. A. Compendium of Material Composition Data for Radiation Transport Modeling. Tech. Rep., Pacific Northwest National Laboratory, Richland (2011).
- [117] Lloyd-Smith, J. O. Maximum Likelihood Estimation of the Negative Binomial Dispersion Parameter for Highly Overdispersed Data, with Applications to Infectious Diseases. *PLOS ONE* **2**, e180 (2007).
- [118] Jaynes, E. T. Information theory and statistical mechanics. *Phys. Rev.* **106**, 620–630 (1957).
- [119] Brooks, S. P. & Gelman, A. General Methods for Monitoring Convergence of Iterative Simulations. *J. Comput. Graph. Stat.* **7**, 434–455 (1998).
- [120] Breitenmoser, D., Stabilini, A., Kasprzak, M. M. & Mayer, S. Source quantification by mobile gamma-ray spectrometry systems: A Bayesian approach (Dataset) (2025).
- [121] Breitenmoser, D., Cerutti, F., Butterweck, G., Kasprzak, M. M. & Mayer, S. FLUKA user routines for non-proportional scintillation simulations (2023).

**Acknowledgements.** We gratefully acknowledge the support by the members of the National Emergency Operations Centre (NEOC), the Swiss Armed Forces, specifically the Swiss Air Force and the Nuclear, Biological, Chemical, Explosive Ordnance Disposal and Mine Action Centre of Excellence (NBC-EOD), as well as the Expert Group Airborne Gamma Spectrometry for their support in conducting the radiation measurements described in this study. Our sincere thanks go to Gernot Butterweck for his invaluable scientific expertise and support during the measurements, as well as for his role in supervision. Finally, we extend our gratitude to Dominik Werthmüller for his technical support in running the Monte Carlo simulations on the computer cluster at the Paul Scherrer Institute. This research was partially supported by the Swiss Federal Nuclear Safety Inspectorate (grant no. CTR00836 & CTR00491).

**Author contributions.** D.B. conceptualized the work, designed the methodology, performed the investigations, curated and analyzed the data, developed the software, validated and visualized the results, and administered the project. D.B. wrote the original draft of the manuscript, and together with A.S., M.M.K. and S.M. reviewed and edited it. A.S. contributed to the investigations. S.M. supervised the project and acquired funding.

**Competing interests.** The authors declare no competing interests.

**Additional information.** The online version contains supplementary material.